Biophysical Journal, Volume *113*

Supplemental Information

Enhanced Dynamics of Confined Cytoskeletal Filaments Driven by Asymmetric Motors

Arvind Ravichandran, Gerrit A. Vliegenthart, Guglielmo Saggiorato, Thorsten Auth, and Gerhard Gompper

CONTENTS

S.I. HYBRID BROWNIAN DYNAMICS

A. Initial Condition

The initial distribution of microtubules (MTs) is straightforward, because the inter-MT potential allows for overlap. First, we pick a random point within the circle defined by the confinement wall, which will potentially be the center of mass of a new MT. Next, we pick a random orientation, and check if the MT intersects with the confining wall. If it does not, we place the MT and proceed to placing the next MT until the necessary number of MTs are placed within the confinement. High overlap penalties tend to remove overlaps within a few thousand molecular dynamics steps, even at high densities.

B. Microtubules and Motors

There are two stochastic processes in our simulations. The first is the Gaussian distributed random displacements, $\delta \boldsymbol{r}_i(t)$, and rotations, $\delta \boldsymbol{p}_i(t)$ of MTs. This process is discussed in the main text. The second is the selection of the attachment position of the motor arms.

At each time step, the distances between beads on neighbouring MTs are checked. If the number of motors attached in the system is less than the predefined number of motors in the entire system, N_{m}, bead pairs that have inter-particle distance smaller than the threshold distance, d_{t}, are picked randomly, and motors are attached between them. The motors act as harmonic bonds with stiffness k_{m}, and energy, $U_{\mathrm{m}} = k_{\mathrm{m}} d^2/2$.

A motor arm that is attached to a MT walks with velocity v_{m} until the distance between the two motor arms reaches the stall length, d_{s}. For extensions beyond d_{s}, the motor arms stop walking. If the motor extension is larger than d_{t}, both arms of the motor detach simultaneously (Fig. S1).

Motion of the motor arms also depends on whether the motors are dimeric or tetrameric. Dimeric motors have one randomly picked anchored motor arm, which remains anchored to one MT until the motor extension is larger than d_{t}. The other motor arm walks on the MT with the velocity shown in Fig. S1, as do both arms of a tetrameric motor. We have no stochastic motor detachment rate, since kinesin molecules are known to be very processive [1].

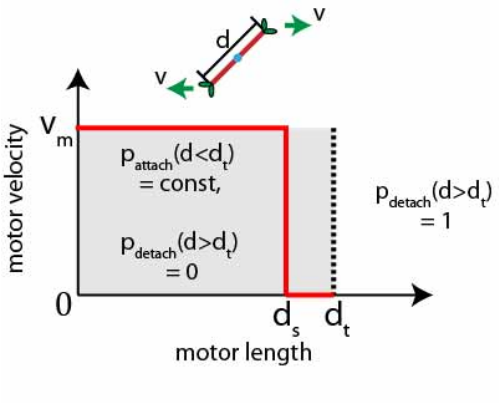

FIG. S1. Motors bind to neighbouring MTs with a constant probability if their length, d, is less than threshold distance, d_{t}, until the predefined number of attached motors in the system, N_{m} is reached. Motors that are longer than d_{t} detach. If the motor length is less than the stall length, *i.e.* for $d < d_{\mathrm{s}}$, active motor arms move with constant velocity, v_{m}.

C. Iteration

The overall Brownian dynamics scheme is:

1. Compute forces and torques due to MT attraction and repulsion.

2. If the number of attached motors is less than N_{m}, look for beads on two different MTs which are closer than d_t, and attach motor arms to these MT pairs. If motors are active, *i.e.*, $d < d_{\mathrm{s}}$, displace each arm by $v_{\mathrm{m}}\delta t$ along the polar direction of the MT to which it is attached.

3. Calculate forces and torques on the MTs due to motors and confinement. Add these values to those obtained from 1.

4. Move MTs based on their respective forces and torques.

5. Update motor arm positions, such that the positions of the arms are conserved after step 4 on the MTs from before step 4. Remove the motors that are stretched beyond the motor threshold, *i.e.*, $d > d_{\mathrm{t}}$, and those motors that contain arms that have walked off the MT.

All the data collected from systems has been measured after the simulations have run for at least $1.5 \times 10^3\tau$, where τ is the onset of the activity time scale discussed in the main text.

S.II. POTENTIALS

MT dynamics occurs either because of forces from the motors, the inter-MT potential or the interaction between MTs and the wall.

A. Motors

Consider two MTs, i and j, each of length, L, with orientations $\boldsymbol{p}_i$ and $\boldsymbol{p}_j$, which correspond with the directions of motor arm motion, and center-of-masses $\boldsymbol{r}_i$ and $\boldsymbol{r}_j$. Note that orientation vectors $\boldsymbol{p}_i$ and $\boldsymbol{p}_j$ are necessarily unit vectors. They are parametrised by contour variables s_i and s_j that equal 0 and 1 at the negative and positive ends of the MTs respectively. A motor that crosslinks these MTs will have arms at positions $\boldsymbol{m}_i$ and $\boldsymbol{m}_j$ on MTs i and j respectively, with motor lengths $|\boldsymbol{m}_{ij}| = |\boldsymbol{m}_j - \boldsymbol{m}_i|$. We can write a motor arm position, $\boldsymbol{m}_i$ using,

$$\boldsymbol{m}_i = \boldsymbol{r}_i + L s_i \boldsymbol{p}_i. \tag{S1}$$

Since the motor is treated as a harmonic spring, the motor energy can be written as,

$$U_\mathrm{m} = \begin{cases} \dfrac{1}{2} k_\mathrm{m} |\boldsymbol{m}_{ij}|^2, & |\boldsymbol{m}_{ij}| \leq d_\mathrm{t} \\ 0, & |\boldsymbol{m}_{ij}| > d_\mathrm{t} \end{cases}, \tag{S2}$$

B. Inter-MT potential

MTs are simulated as rigid rods of length L and radius r_min. They are composed of linearly arranged particles (beads). In order for MTs to "feel" each other as contiguous entities, and not a collection of discrete beads, the beads overlap. We placed a bead every $0.5r_\mathrm{min}$, such that $L = 0.5r_\mathrm{min}\left(N_\mathrm{B} - 1\right)$. Each bead which makes up an MT, interacts with beads from neighbouring MTs with a capped interaction potential, which has an attractive component. The general form of the potential used in our simulation is

$$U(r) = A_R \left(\frac{s^m}{r^m + \alpha^m}\right)^n - A_\mathrm{A} \left(\frac{s^m}{r^m + \alpha^m}\right)^{n/2} \tag{S3}$$

Here, α, A_A and A_R are dependent on overlap penalty, E_R, attraction energy, E_A, and the position of the attractive well, r_min,

$$\alpha = r_\mathrm{min}\left(\left(1+\sqrt{E_\mathrm{R}/E_\mathrm{A}}\right)^{2/n}-1\right)^{-1/m}, \tag{S4}$$

$$A_\mathrm{A} = 2\alpha^{mn/2}s^{-mn/2}E_\mathrm{A}\left(1+\sqrt{E_\mathrm{R}/E_\mathrm{A}}\right), \tag{S5}$$

and

$$A_\mathrm{R} = \frac{A_\mathrm{A}^2}{4E_\mathrm{A}}. \tag{S6}$$

The variable s depends on the length of MTs, L, and the number of particles that makes up this MT, N_B:

$$s = \frac{L}{(N_\mathrm{B}-1)}. \tag{S7}$$

For all simulations, $m = 2$, $n = 8$ and $r_\mathrm{min} = 1$. The exponents of the potential are chosen such that the superposition of multiple, overlapping beads gives a smooth, attractive MT-MT interaction, with a repulsive core. To characterise the potential, instead of looking at interaction energies between particles, we look at interaction energies between MTs in different orientations. In the following examples, one of the MTs (dark blue MT in Figs. S2, S3, S4) is fixed in position, and the position of the other MT is varied. We plot the energy that arises as a result of the superposition of the potentials between beads from the neighbouring MT.

Fig. S2 shows the energy of the two MTs as function of the separation distance, Δx for $E_\mathrm{R} = 6k_\mathrm{B}T$ and $E_\mathrm{R} = 20k_\mathrm{B}T$. We notice that the position of the minimum attraction energy shifts closer to the core of the MT than r_min, because of the superposition of the energy wells of multiple beads. We will call this distance x_min and use it only for the MT sliding example discussed below. We use $E_\mathrm{R} = 20k_\mathrm{B}T$ for all calculations in the main text. At this level of repulsion, the overlap penalty is six fold higher than the energy of attraction, which makes MT crossings rare.

In order to ensure that A_R does not diverge, we take the limit $E_\mathrm{A} \to 0$ for curves marked $E_\mathrm{A} = 0.0$. Because of the manner in which our potential is constructed, the shape of the

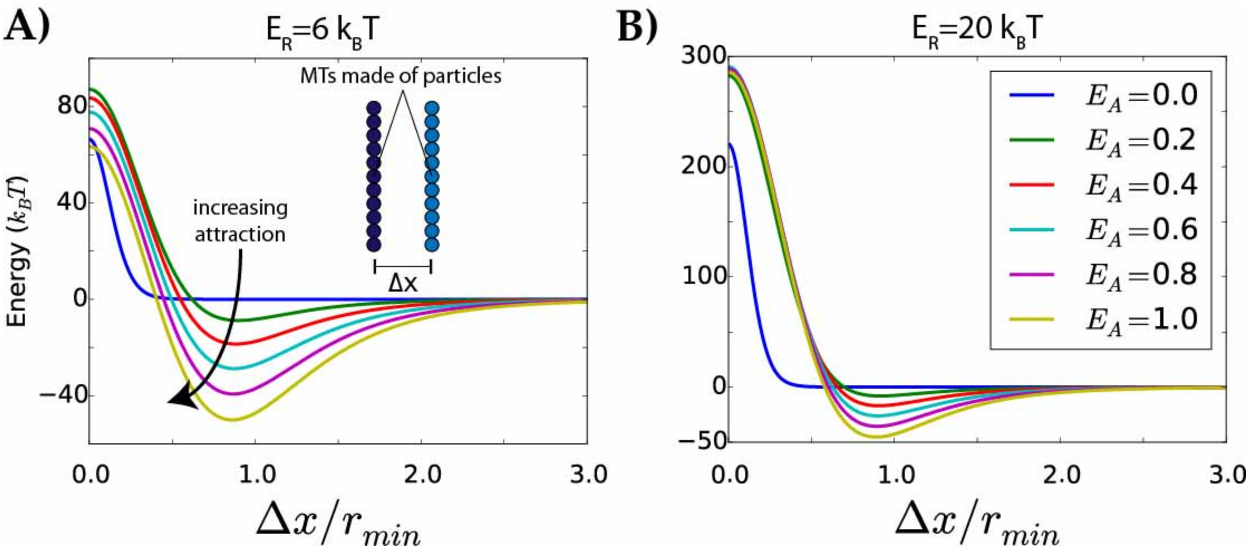

FIG. S2. Inter-MT energy as a function of separation distance, Δx, between an aligned MT pair, for different $E_{\rm A}$ values. Two regimes of repulsion are illustrated: (A) $E_{\rm R} = 6k_{\rm B}T$ and (B) $E_{\rm R} = 20k_{\rm B}T$. Negative energies indicate attraction, and positive energies indicate repulsion. Inset in (A) shows the orientation with which the calculation is conducted.

potential for $E_{\rm A} = 0$ differs substantially from larger values of $E_{\rm A}$ (Fig. S2). We, thus, do not use this potential to simulate systems which are not attractive.

Fig. S3 shows the energy of the MTs as a function of their parallel displacement, Δy. In this instance, we slide two aligned MTs apart, along their longitudinal axis. We keep the orthogonal displacement to be the position where the inter-MT energy is the smallest, $x_{\rm min} = 0.8r_{\rm min}$. The energy increases monotonically as the filaments slide away from each other, since the attractive interactions decrease, as the number of interacting beads decreases. When the centers of masses are separated further than the MT length, the number of interacting beads decreases to 1, and then the energy vanishes as the MTs are moved further away. The values chosen for the attraction energies correspond with the range of cohesion energies for the *in vitro* MT sliding experiment calculated for different PEG concentration [2].

In Fig. S3, two MTs are rotated with respect to each other, with the center beads of both MTs overlapping. For $E_{\rm R} = 6k_{\rm B}T$, and for $E_{\rm A} < 0.6k_{\rm B}T$ the potential is repulsive for all angles. For $E_{\rm R} = 6k_{\rm B}T$, $E_{\rm A} > 0.6k_{\rm B}T$, the potential has minima in two orientations. One must keep this in mind before using this potential for smaller overlap penalties, which can

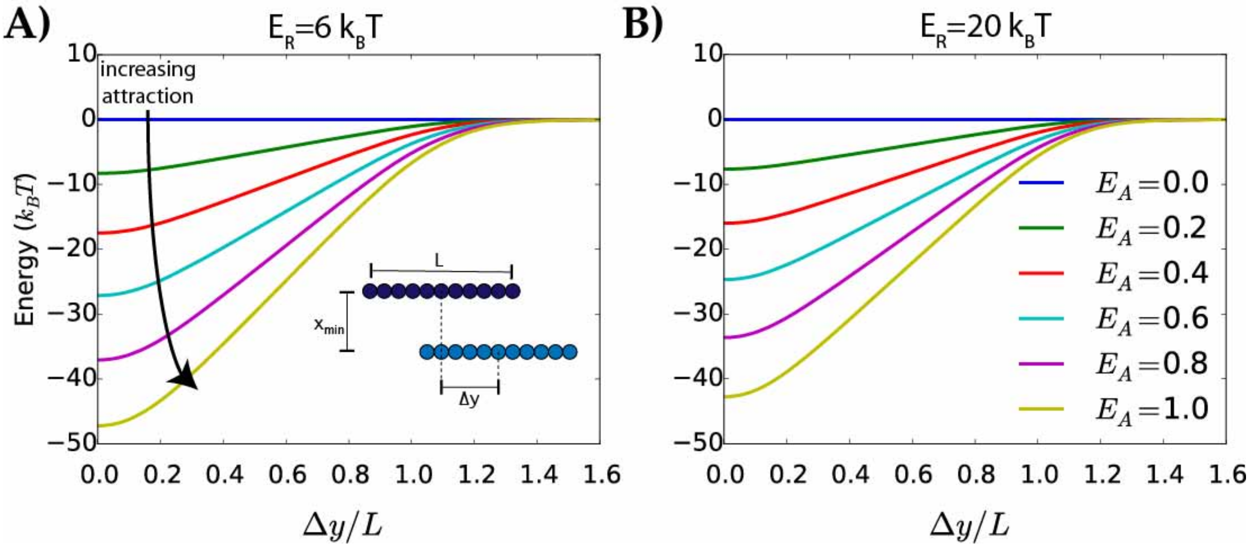

FIG. S3. Inter-MT energy as a function of parallel displacement between MTs' centers of masses, Δy, for different E_{A} values. The orthogonal displacement is set to be $x_{\min}$, the position of the energy well, seen in Figure S2. We illustrate two regimes of repulsion: (A) $E_{\mathrm{R}} = 6k_{\mathrm{B}}T$ and (B) $E_{\mathrm{R}} = 20k_{\mathrm{B}}T$. In both cases $x_{\min} = 0.8r_{\min}$. Inset in (A) shows the orientation with which the calculation is conducted.

lead to clustering of filaments due to such stable orientations. We avoid this issue here by using $E_{\mathrm{R}} = 20k_{\mathrm{B}}T$. This makes the potential repulsive for all values of E_{A}.

C. MT-wall interaction

Self-propelled, active particles are known to accumulate at confinement walls [3]. In order to stabilise a layer of MTs close to the wall, in our work, we adhere MTs to the wall using an attractive wall potential. Beads which make up the MTs interact with the wall with a 6-12 Lennard Jones potential,

$$U_{\mathrm{w}}(r) = \begin{cases} 4\epsilon\left[\left(\frac{r_{\min}}{r}\right)^{12} - \left(\frac{r_{\min}}{r}\right)^{6}\right] & r \leqslant 3r_{\min} \\ 0 & r > 3r_{\min} \end{cases}, \tag{S8}$$

where r is the distance between a bead and the wall, and $r_{\min}$ is the position of the attractive energy well. We choose the same range, $3r_{\min}$, for MT-MT interactions and MT-wall interactions. Superposition of these potentials between all the beads that make up an MT

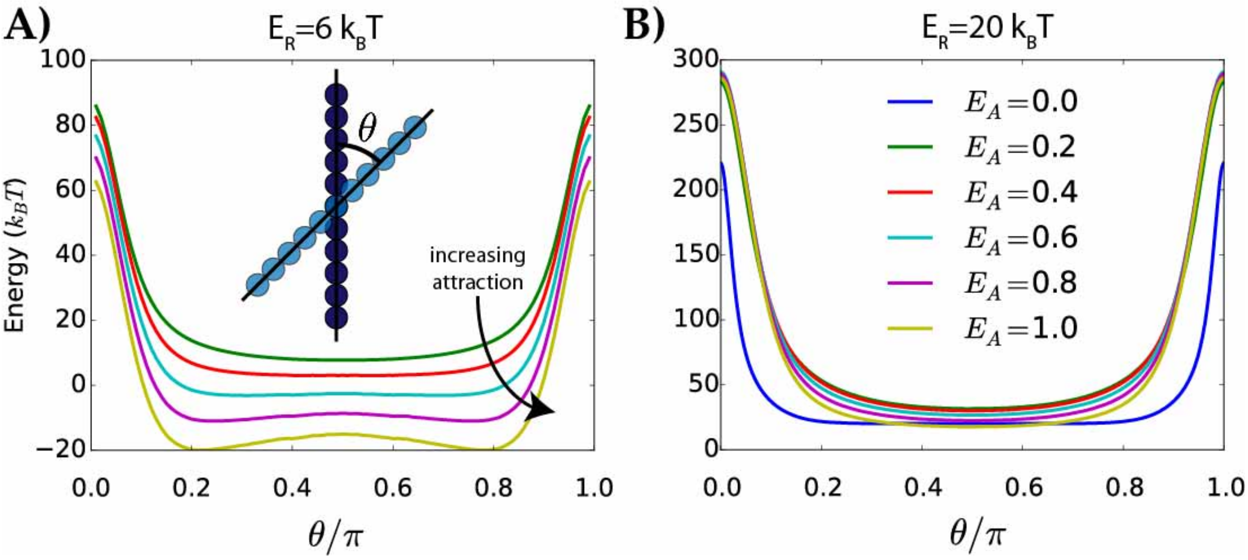

FIG. S4. Inter-filament energy as a function of increasing the angle of crossing between two overlapping filaments, θ, for different E_{A} values. We illustrate two regimes of repulsion: (A) $E_{\mathrm{R}} = 6k_{\mathrm{B}}T$ and (B) $E_{\mathrm{R}} = 20k_{\mathrm{B}}T$. Inset in (A) shows the orientation with which the calculation is conducted.

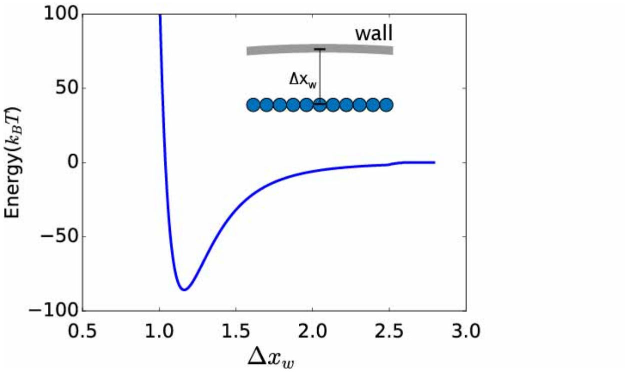

FIG. S5. Interaction energy of MT with the wall with a 6-12 Lennard Jones potential. $\epsilon_{\mathrm{w}} = 8k_{\mathrm{B}}T$, $\sigma_{\mathrm{w}} = r_{\mathrm{min}}$. Δx_{w} are given in units of r_{min}.

and the wall gives the curve shown in Fig. S5.

A comparison of the energies in Fig. S5, with those of Figs. S2, S3 and S4, shows that the attractive MT-wall interaction energy is sufficient to stabilise a layer of partially overlapping MTs close to the wall [4], because the level of attraction is larger (-90 $k_{\mathrm{B}}T$) than the other energies (attractive or repulsive) involved in the system.

S.III. PARAMETERS

The primary parameters varied in the simulations are attraction energy, E_{A}, and number of motors, N_{m}. Despite having taken a step toward capturing cellular scale phenomena by marrying three distinct components of very different length scales, we have tried to capture biologically accurate lengths in the simulation (Table S1). However, in our coarse-grained model we chose constant motor speeds, 3.6 times faster than motor speeds from single molecule experiments. In so doing we remove the force dependency on motor speed and shift the focus from the loads on individual motors to conduct MT sliding. Instead, we use motors as coarse-grained entities that propel MTs based on the MT pair's orientation. In order to traverse another order of magnitude in length scale and simulate MTs in cell-sized confinements, such coarse-graining choices need to be explored.

A complete list of parameters used in our simulations is given in Table S1. We match the parameters to biological values when possible. Note that the viscosity, η, is linked to the friction coefficient, γ_0, used in the dynamical equations [5].

We choose the MT diameter (r_{min}) and activity time scale (τ) as the characterstic length and time units, for defining dimensionless parameters, respectively. The thermal energy, $k_{\mathrm{B}}T$, is the characterstic energy scale. The dimensionless form of the parameters are collected in Table S2.

The results of a systematic study of the effect of the various parameters on the global structure and dynamics of MTs for both tetrameric and dimeric motor systems are summarised below. This concerns, in particular, the effect of varying area fraction, confinement size, motor concentration, motor spring constant and motor velocity.

Each MT is composed of 11 overlapping beads. For all the cases shown in the main text, there are 927 MTs within the confinement. If we define the MT diameter to be r_{min}, then the MTs have an aspect ratio of 5. In order to determine the area fraction of penetrable MTs within the confinement, we consider the effective bead radius to be $r_{\mathrm{eff}} = 0.8 r_{\mathrm{min}}$ (Fig. S21). For 927 MTs, the effective packing fraction of MTs is given by $N_{\mathrm{f}} r_{\mathrm{eff}} L / \pi R_{\mathrm{W}}^2 = 0.74$.

TABLE S1. Simulation Parameters

Parameter	Symbol	Value	Notes/Biological Values
Thermal energy	$k_{\mathrm{B}}T$	4.11 pN nm	Room Temperature
MT length	L	0.125 μm	2.5 ± 1.4 μm [6]
MT diameter	r_{min}	25 nm	25 nm [7]
Confinement radius	R_{W}	1 μm	Oocyte $\sim 200\mu$m [4]
Repulsive peak	E_{R}	$20k_BT$	Chosen
MT Attractive well	E_{A}	$0.2 - 1.0k_{\mathrm{B}}T$	*in vitro* experiments [2]
Confining wall attraction	ϵ_{w}	$8.0k_BT$	Chosen
Confining wall range	σ_{w}	25 nm	Chosen
Fluid viscosity	η	1 Pa s	Cytoplasmic viscosity [8]
Maximum motor speed	v_{m}	6.5 μm/s	Single motor speed ~ 1.8 μm/s [9]
Maximum motor extension	d_{t}	25 nm	80 nm [10]
Motor stall force	f_{s}	7.83 pN	5 pN [11]
Motor spring constant	k_{m}	0.33 pN/nm	Single kinesin molecule [12]

A. Packing fraction

To understand the effect of packing fraction on large scale structures, for both cases of motors, we performed simulations for 649, 834, 927, 1020, and 1205 MTs. The structures for these packing fractions are shown in Fig. S6. With increasing area fraction of MTs polarity sorting becomes more prominent, and polar aligned, structured domains become more pronounced for both types of motors. The diffusion of MTs are hindered for larger densities for lag times less than τ, for both motor models. This is clear when we compare the dynamics of motor-driven systems at higher densities with the passive system at an area fraction of 0.74. However, we observed similar levels of activity for dimeric motors, across all densities, for lag times larger than τ. For tetrameric motors, denser systems leads to

TABLE S2. Dimensionless Groups

Parameter	Symbol	Value
Area fraction	$\frac{N_\mathrm{f} r_\mathrm{eff} L}{\pi R_\mathrm{W}^2}$	0.74
MT aspect ratio	$\frac{L}{r_\mathrm{min}}$	5
Confinement diameter	$\frac{R_\mathrm{W}}{r_\mathrm{min}}$	80
Motor to MT ratio	$\frac{N_\mathrm{m}}{N_\mathrm{f}}$	1
Maximum motor speed	$\frac{v_\mathrm{m}\tau}{r_\mathrm{min}}$	50
Maximum motor extension	$\frac{d_\mathrm{t}}{r_\mathrm{min}}$	1
Motor stall force	$\frac{f_\mathrm{s} r_\mathrm{min}}{k_\mathrm{B} T}$	47.7
Motor spring constant	$\frac{k_\mathrm{m} d_\mathrm{t}}{f_\mathrm{s}}$	1

lower levels of activity across all lag times (Fig. S7).

B. Confinement diameter

Simulations of five different confinement diameters show an increase in the number of polar aligned domains with increasing confinement size for both the dimeric and tetrameric motor systems (Fig. S8). The active displacements increase with increasing confinement diameter for both motor systems, at large lag times, (Lag time/τ) $\geq 10^2$ (Fig. S9). As discussed in the main text, the MSD of MTs plateaus at the confinement radius. We observe larger active displacements for larger confinements, because MTs are not yet hindered by the confinement at this time scale.

C. Motor concentration

Motor concentration has the strongest effect on the structures observed, and is one of the primary parameters discussed in the main text. It is also a parameter that is accessible in experiments. At low motor concentrations, $N_\mathrm{m}/N_\mathrm{f} = 0.5$, the polarity sorting results in large polar-aligned domains for both dimeric and tetrameric motors, and there are not enough motors to induce large-scale motion. For $N_\mathrm{m}/N_\mathrm{f} = 3$, there is a higher proportion of MTs which are aligned with the confining wall for the dimeric motor system. Higher motor concentration further emphasises the bundling of MTs in the tetrameric motor system (Fig. S11).

Activity increases with increasing motor concentrations, because there are more active elements to slide MTs. However, this is more prominent in the dimeric motors than in the tetrameric motor system (Fig. S11). For dimeric motors, we show the onset of a plateau in the MSD upon reaching R_W^2, where a significant proportion of MTs' displacements are limited by the confining wall (Fig. S11C). On this time scale, we do not observe this for the tetrameric motors, because their dynamics is slower (Fig. S11D).

D. Motor spring constant

Increasing motor spring strength does not induce any appreciable change in overall structure of the system for both motor systems (Fig. S12). However, increasing the motor spring constant increases active displacements of MTs for both dimeric and tetrameric motor systems. This is the most effective method to diminish the difference in MT activity between the dimeric and tetrameric motors (Fig. S13).

E. Motor velocity

Increasing motor velocity does not change the overall structure of the system for both motor systems (Fig. S14). However, it decreases the crossover time between diffusion and activity dramatically for the dimeric motor system (Fig. S15). The differences between the tetrameric and dimeric motors are greatly enhanced for higher motor velocities, since the crossover time appears to be conserved for the tetrameric motors, possibly due to the lack of antialigned MTs. In the main text, we have used the motor velocity that is biologically motivated.

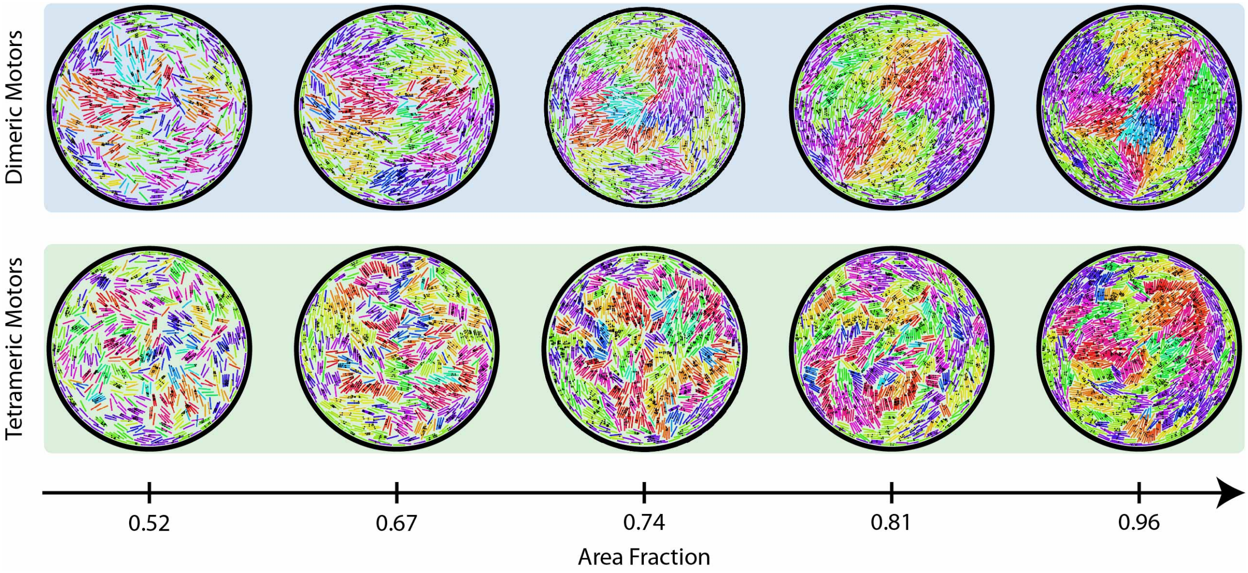

FIG. S6. Snapshots of steady state structures for different area fractions for dimeric and tetrameric motors. The area fractions correspond to 649, 834, 927, 1020, and 1205 MTs within the confinement. All packing fraction are computed using $r_{\mathrm{eff}} = 0.8 r_{\mathrm{min}}$. 927 MTs are used for all results in the main text. For these simulations, $R_{\mathrm{W}}/L = 8$, $\epsilon_{\mathrm{w}} = 8 k_{\mathrm{B}} T$, $E_{\mathrm{A}} = 0.2$, $v_{\mathrm{m}} \tau / r_{\mathrm{min}} = 50$, $k_{\mathrm{m}} d_{\mathrm{t}} / f_{\mathrm{s}} = 1$ and $N_{\mathrm{m}}/N_{\mathrm{f}} = 1$.

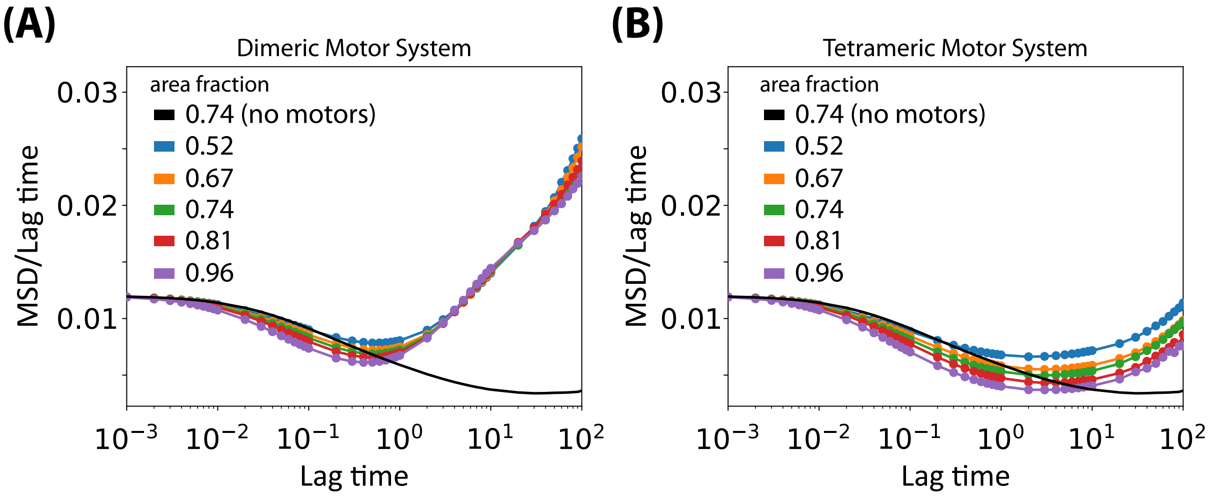

FIG. S7. MSD/Lag time for different area fractions for dimeric and tetrameric motors. The area fractions correspond to 649, 834, 927, 1020, and 1205 MTs within the confinement. MSD is normalised by L^2 and lag time is normalised by τ. $R_{\mathrm{W}}/L = 8$, $\epsilon_{\mathrm{w}} = 8 k_{\mathrm{B}} T$, $E_{\mathrm{A}} = 0.2 k_{\mathrm{B}} T$, $v_{\mathrm{m}} \tau / r_{\mathrm{min}} = 50$, $k_{\mathrm{m}} d_{\mathrm{t}} / f_{\mathrm{s}} = 1$ and $N_{\mathrm{m}}/N_{\mathrm{f}} = 1$.

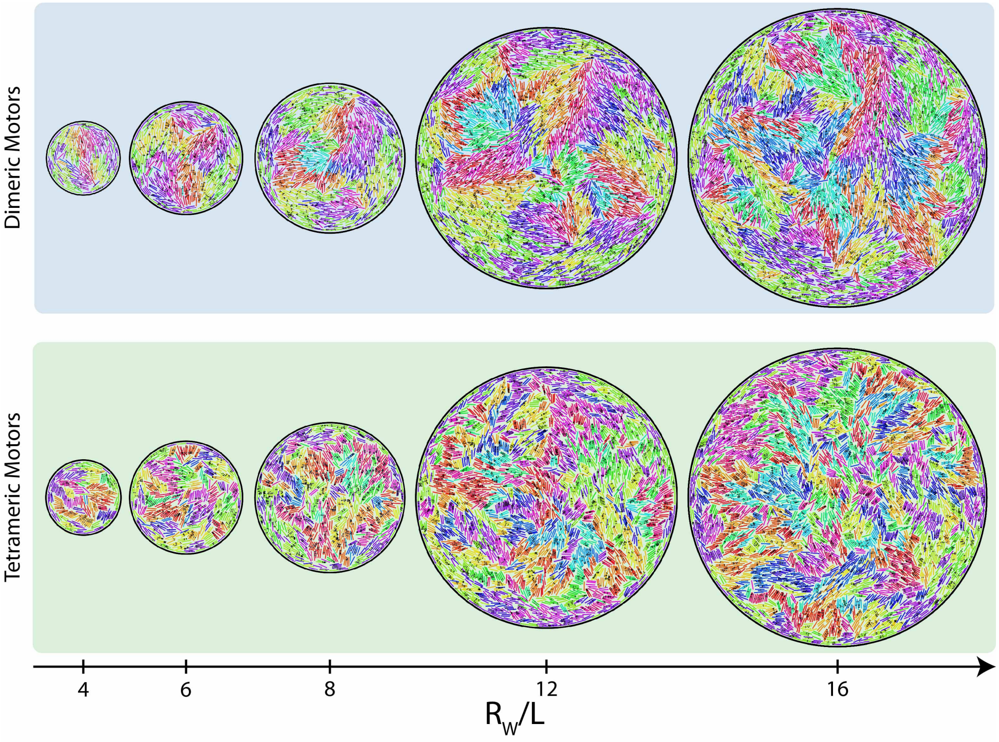

FIG. S8. Snapshots of steady state structures for different diameters of confinement relative to r_{min}. We use $R_{\mathrm{W}}/L = 8$ for all findings in the main text. The area fraction is kept constant at 0.74, $\epsilon_{\mathrm{w}} = 8k_{\mathrm{B}}T$, $E_{\mathrm{A}} = 0.2k_{\mathrm{B}}T$, $k_{\mathrm{m}}d_{\mathrm{t}}/f_{\mathrm{s}} = 1$, $v_{\mathrm{m}}\tau/r_{\mathrm{min}} = 50$ and $N_{\mathrm{m}}/N_{\mathrm{f}} = 1$.

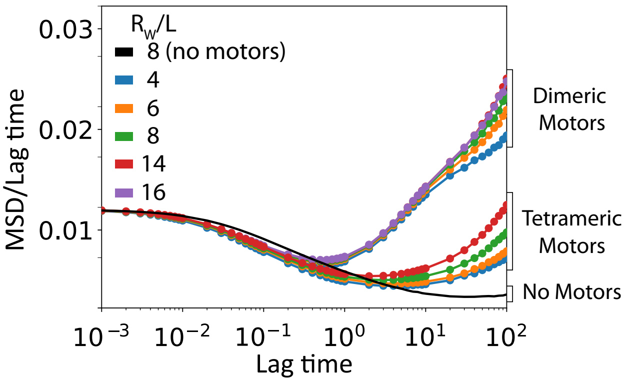

FIG. S9. MSD/Lag time for different confinement diameters. MSD is normalised by L^2 and lag time is normalised by τ. The area fraction is kept constant at 0.74, $\epsilon_{\mathrm{w}} = 8k_{\mathrm{B}}T$, $E_{\mathrm{A}} = 0.2k_{\mathrm{B}}T$, $k_{\mathrm{m}}d_{\mathrm{t}}/f_{\mathrm{s}} = 1$, $v_{\mathrm{m}}\tau/r_{\mathrm{min}} = 50$ and $N_{\mathrm{m}}/N_{\mathrm{f}} = 1$. Note that we use more MTs and more motors in systems with larger confinements.

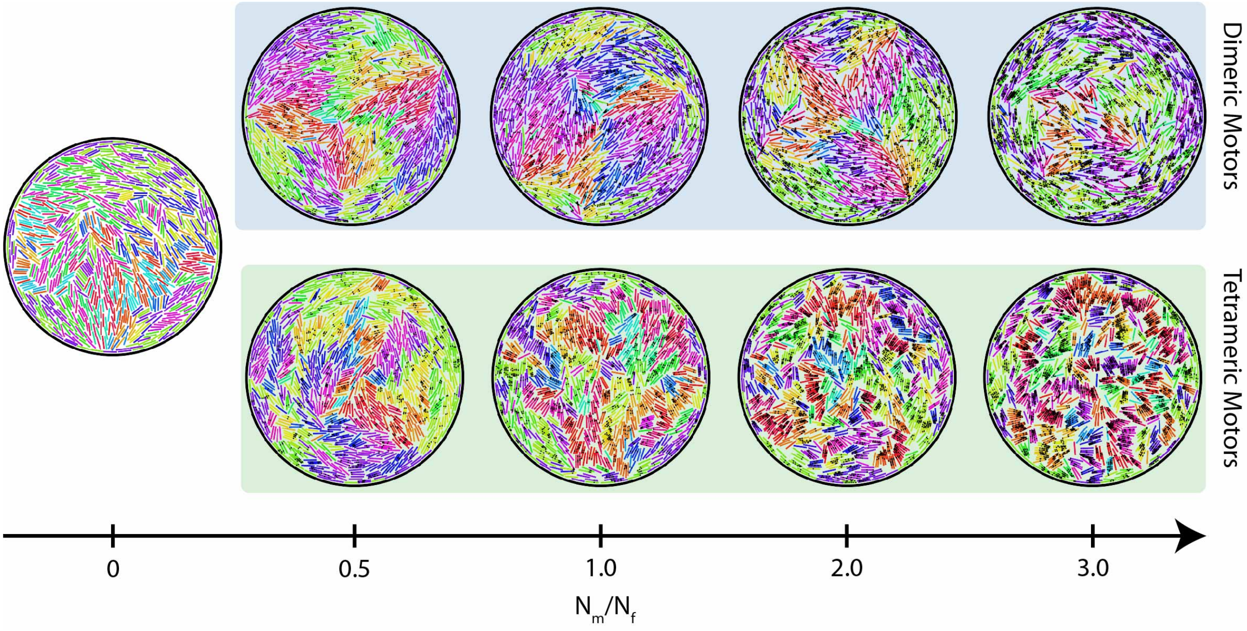

FIG. S10. Snapshots of steady state structures for different $N_\mathrm{m}/N_\mathrm{f}$ for dimeric and tetrameric motors. We use $N_\mathrm{m}/N_\mathrm{f} = 1$ for all findings in the main text. The area fraction is 0.74, $R_\mathrm{W}/L = 8$, $\epsilon_\mathrm{w} = 8k_\mathrm{B}T$, $E_\mathrm{A} = 0.2k_\mathrm{B}T$, $k_\mathrm{m}d_\mathrm{t}/f_\mathrm{s} = 1$ and $v_\mathrm{m}\tau/r_\mathrm{min} = 50$.

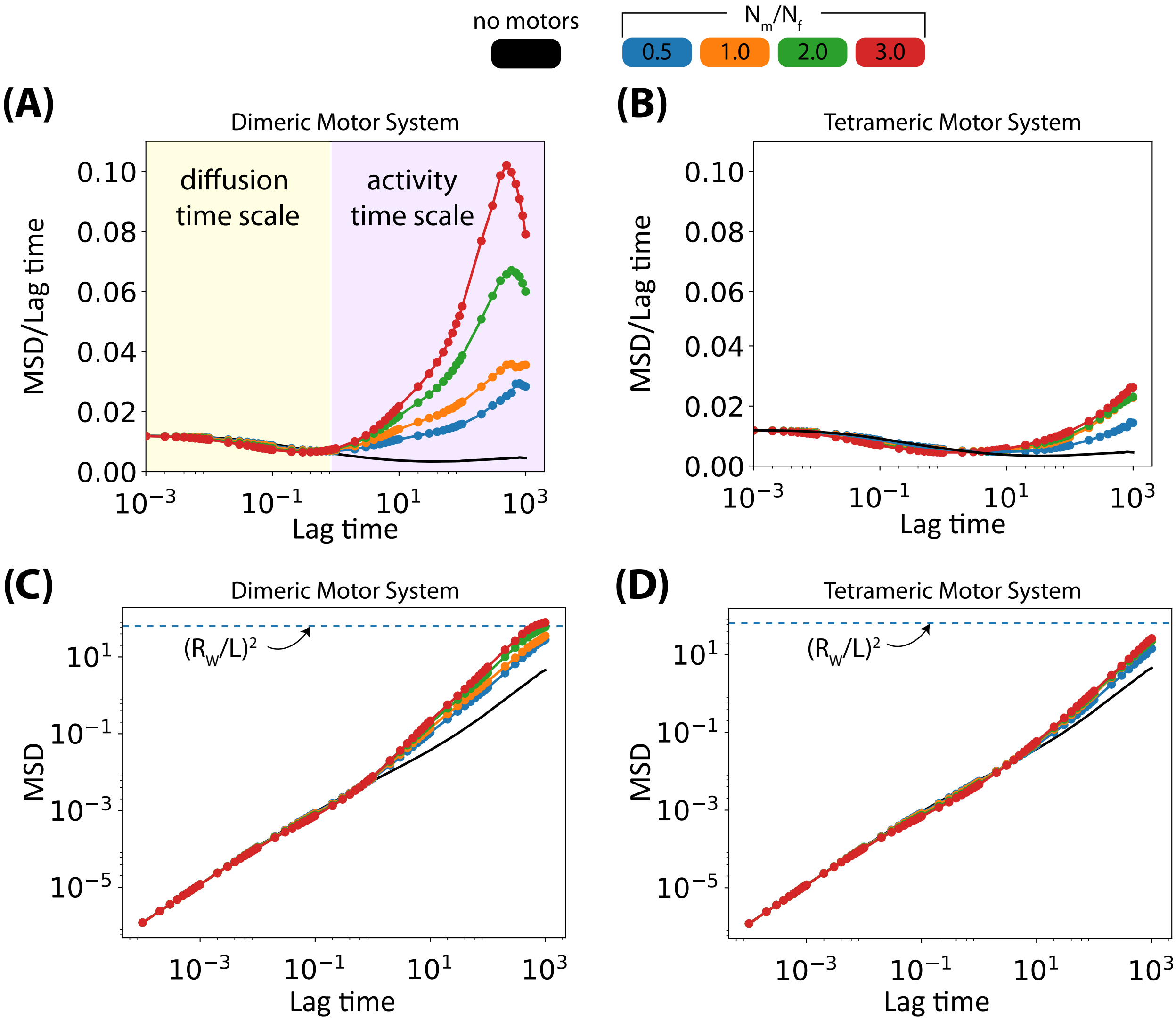

FIG. S11. MSD/Lag time for different $N_\mathrm{m}/N_\mathrm{f}$ for dimeric (A) and tetrameric (B) motors. MSD vs lag times for dimeric (C) and tetrameric (D) motors. The squared wall radius is represented by the dotted blue line in (C) and (D). MSD is normalised by L^2 and lag time is normalised by τ. The area fraction is 0.74, $R_\mathrm{W}/L = 8$, $\epsilon_\mathrm{w} = 8k_\mathrm{B}T$, $E_\mathrm{A} = 0.2k_\mathrm{B}T$, $k_\mathrm{m}d_\mathrm{t}/f_\mathrm{s} = 1$ and $v_\mathrm{m}\tau/r_\mathrm{min} = 50$.

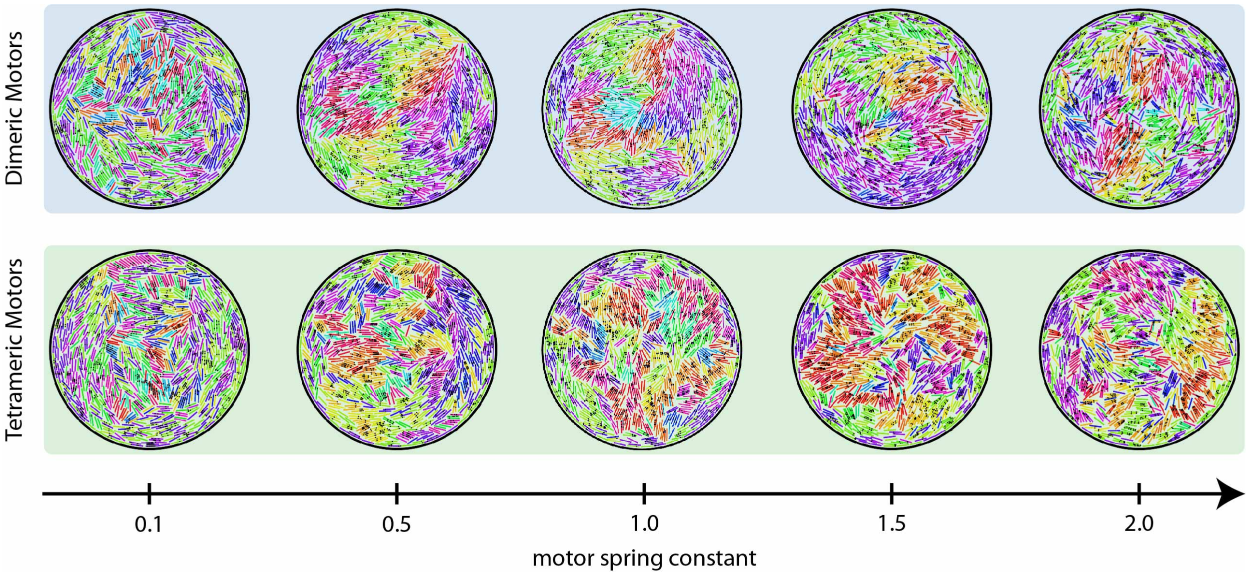

FIG. S12. Snapshots of steady state structures for different $k_{\mathrm{m}}d_{\mathrm{t}}/f_{\mathrm{s}}$. A motor spring constant of $k_{\mathrm{m}}d_{\mathrm{t}}/f_{\mathrm{s}} = 1$ was used for all findings in the main text. The area fraction is 0.74, $R_{\mathrm{W}}/L = 8$, $\epsilon_{\mathrm{w}} = 8k_{\mathrm{B}}T$, $E_{\mathrm{A}} = 0.2k_{\mathrm{B}}T$, $k_{\mathrm{m}}d_{\mathrm{t}}/f_{\mathrm{s}} = 1$, $v_{\mathrm{m}}\tau/r_{\mathrm{min}} = 50$ and $N_{\mathrm{m}}/N_{\mathrm{f}} = 1$.

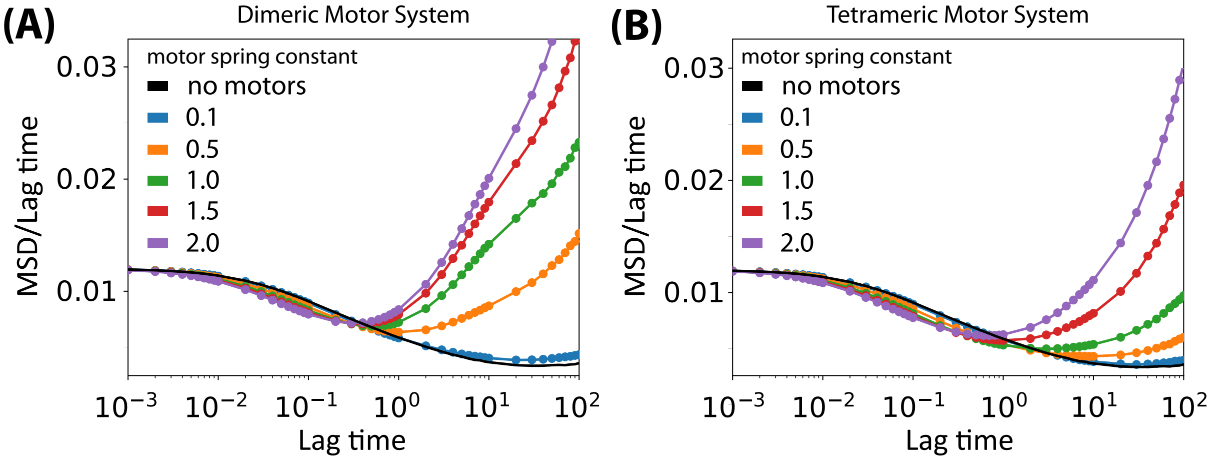

FIG. S13. MSD/Lag time for different $k_{\mathrm{m}}d_{\mathrm{t}}/f_{\mathrm{s}}$. MSD is normalised by L^2 and lag time is normalised by τ. The area fraction is 0.74, $\epsilon_{\mathrm{w}} = 8k_{\mathrm{B}}T$, $E_{\mathrm{A}} = 0.2k_{\mathrm{B}}T$, $v_{\mathrm{m}}\tau/r_{\mathrm{min}} = 50$, $R_{\mathrm{W}}/L = 8$ and $N_{\mathrm{m}}/N_{\mathrm{f}} = 1$.

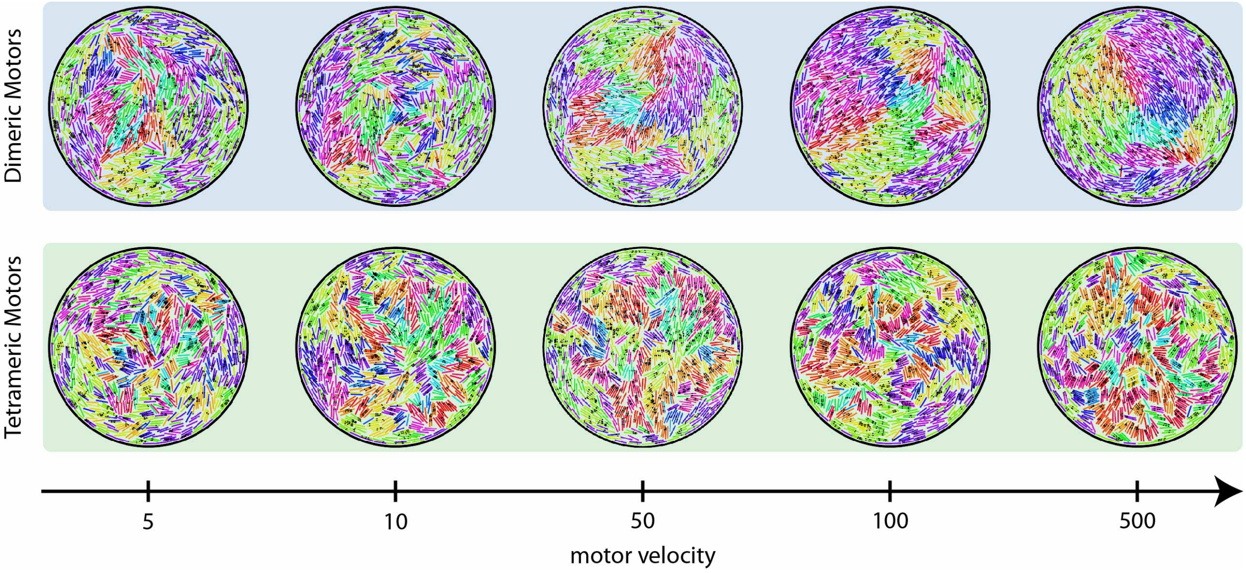

FIG. S14. Snapshots of steady state structures for different $v_\mathrm{m}\tau/r_\mathrm{min}$. A motor velocity of $v_\mathrm{m}\tau/r_\mathrm{min} = 50$ was used for all findings in the main text. The area fraction is 0.74, $R_\mathrm{W}/L = 8$, $\epsilon_\mathrm{w} = 8k_\mathrm{B}T$, $E_\mathrm{A} = 0.2k_\mathrm{B}T$, $k_\mathrm{m}d_\mathrm{t}/f_\mathrm{s} = 1$ and $N_\mathrm{m}/N_\mathrm{f} = 1$.

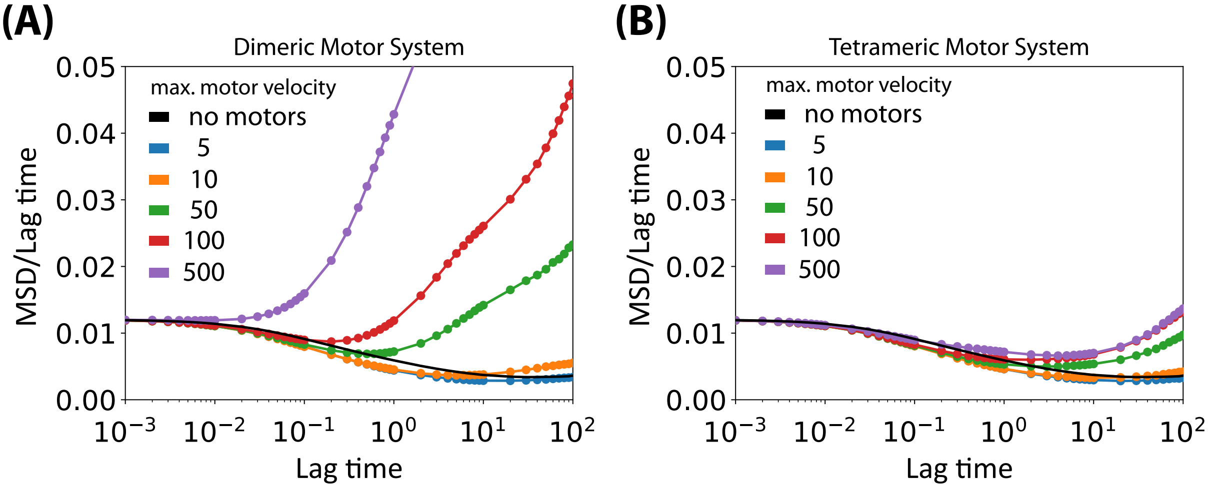

FIG. S15. MSD/Lag time for different $v_\mathrm{m}\tau/r_\mathrm{min}$. MSD is normalised by L^2 and lag time is normalised by τ. The area fraction is 0.74, $R_\mathrm{W}/L = 8$, $\epsilon_\mathrm{w} = 8k_\mathrm{B}T$, $E_\mathrm{A} = 0.2k_\mathrm{B}T$, $k_\mathrm{m}d_\mathrm{t}/f_\mathrm{s} = 1$ and $N_\mathrm{m}/N_\mathrm{f} = 1$.

S.IV. LOCAL POLAR ORDER PARAMETER

In order to characterise a MT's neighbourhood, we define a pairwise motor partition function, $q_{ij}(\boldsymbol{r}_i, \hat{\boldsymbol{p}}_i, \boldsymbol{r}_j, \hat{\boldsymbol{p}}_j)$ as [13]

$$q_{ij} = \rho^2 \int_{-1/2}^{1/2} ds_i \int_{-1/2}^{1/2} ds_j e^{-\beta U_{\mathrm{m}}(|\boldsymbol{m}_{ij}|)}, \tag{S9}$$

where ρ is the linear density of binding sites on a single MT, and s_i and s_j parametrise the positions of motor arms on MTs i and j, respectively (Eq. S1).

The quantity weights pairwise interactions of MTs on the basis of motor binding site availability, which is a function of MT pair's relative orientation and distance. For instance, q_{ij} becomes significant only for pairs of MTs in close proximity, and $q_{ij} = 1$ when they are perfectly overlapping each other. When two MTs are sufficiently far away, such that no motors can interact between them, $q_{ij} = 0$, and the MTs are said to be outside motor range (Fig. S16(A and E)). Since the motor energy $U_{\mathrm{m}}(|\boldsymbol{m}_{ij}|)$ increases quadratically with increasing motor extension (Eq. S2), the partition function, q_{ij}, decays rapidly as binding sites for motors on the MTs become farther and less (Figure S16).

For MTs within motor range, we define them to be antialigned if $(\boldsymbol{p}_i \cdot \boldsymbol{p}_j) < 0$ and polar-aligned if $(\boldsymbol{p}_i \cdot \boldsymbol{p}_j) \geq 0$. Weighing $(\boldsymbol{p}_i \cdot \boldsymbol{p}_j)$ by q_{ij} gives a good representation of local polar order, because it invokes the polarity of just the neighbourhood of the MT in question. And the notion of neighbourhood is clearly defined as the availability of motor binding between the MT pair in question. Moreover, by taking the sum of all interacting MTs with MT i, $\psi(i) = \sum_{i \neq j} (\boldsymbol{p}_i \cdot \boldsymbol{p}_j) q_{ij} / \sum_{j \neq i} q_{ij}$, depends solely on the polarity of the neighbourhood of MT i. We employ $\psi(i)$ to find correlations in velocities with the polarity of MT neighbourhood.

Figure S17 shows antiparallel and parallel orientations of MTs at stationary state for systems with dimeric and tetrameric motors, where MTs are coloured based on their local polar order parameter. In the dimeric motor system (Fig. S17A), large polar-aligned MT clusters compose the entire system. Geometric frustration due to the confinement, and the motion of MTs within polar-aligned clusters give rise to an interface of antialigned MTs that is perpetually created and destroyed throughout the simulation. A significant population of motile, antialigned MTs are observed, in particular close to the confining wall. For the system with tetrameric motors (Fig. S17B), static, polar-aligned bundles of strongly attracting MTs make up the system. The strong attraction within aligned bundles hinders the for-

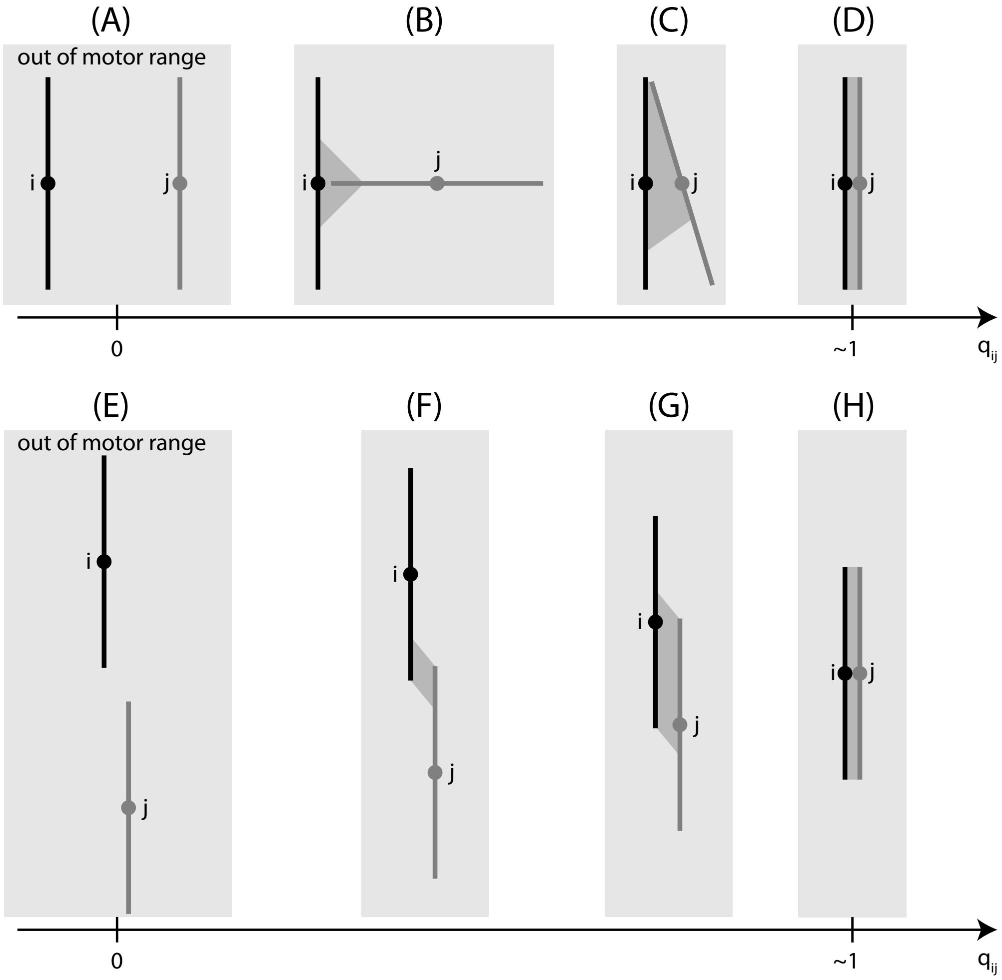

FIG. S16. Pairwise motor partition function, q_{ij}, quantifies the availability of motor binding between MT pairs. (A, B, C and D) shows the effect of rotational degrees of freedom on MT pairs. (E, F, G, H) shows the effect of translational degrees of freedom on MT pairs. The shaded region indicates the region available for motor binding. (D) and (H) are identical and show an instance of near perfect overlap, and availability of motor binding between MT pairs.

mation of interfaces of antialigned MTs. Nevertheless, the confinement hinders the sorting mechanism, such that a considerable population of antialigned MTs is observed. They appear intermittently, and quickly become members of polar-aligned bundles, re-establishing the stationary structure of the system.

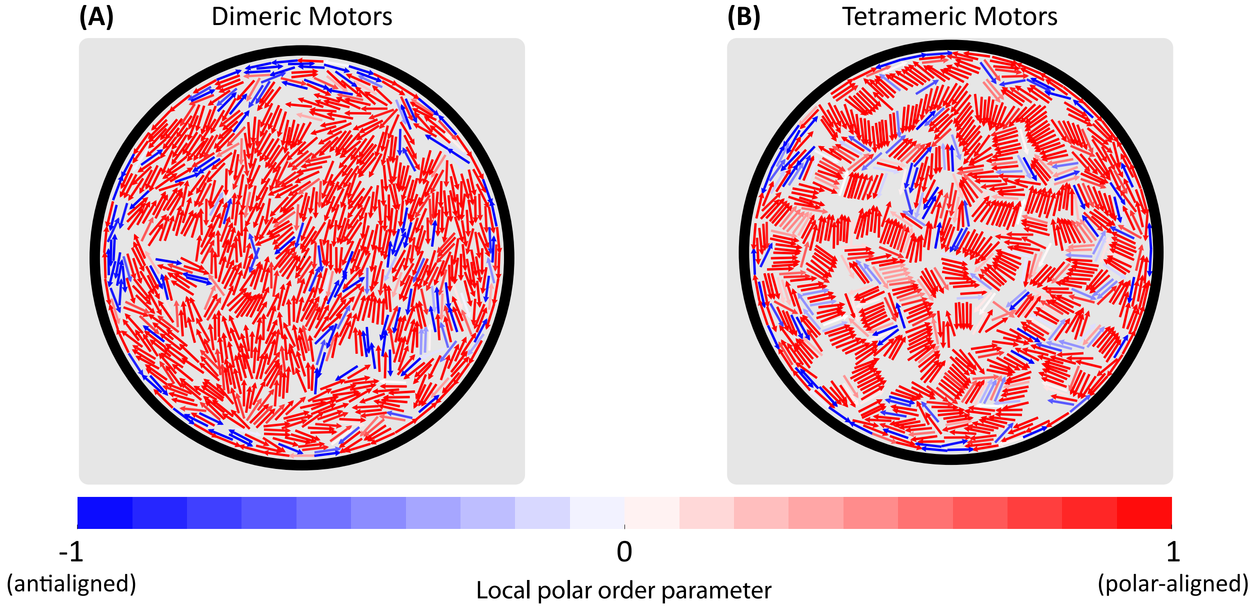

FIG. S17. Stationary configuration of MTs in systems with (A) dimeric and (B) tetrameric motors for $E_A = 1.0k_BT$ and $N_m/N_f = 1$. Arrow heads represent the direction of motor-arm motion on MT. The colour of each arrow represents the local polar orientational order parameter.

S.V. SUPPLEMENTARY FIGURES

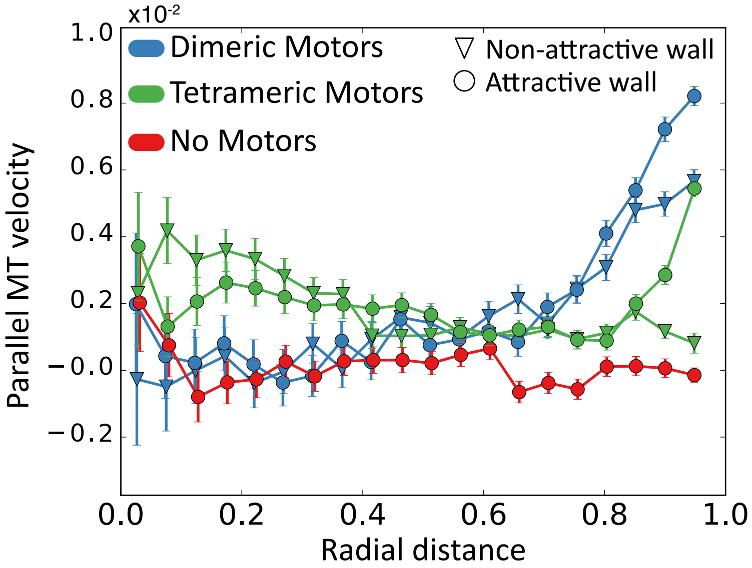

FIG. S18. Parallel MT velocity vs. radial distance for tetrameric, dimeric and passive systems. This is the same as Fig. 9 in the main text, but includes the velocities for the cases with both attractive and non-attractive confining walls. MTs near the confining wall are slower in the systems with the non-attractive walls relative to the systems with the attractive wall. $E_{\mathrm{A}} = 0.2k_{\mathrm{B}}T$ and $N_{\mathrm{m}}/N_{\mathrm{f}} = 1$. Velocities are normalised by L/τ. Radial distance is normalised by confining wall radius, R_{W}.

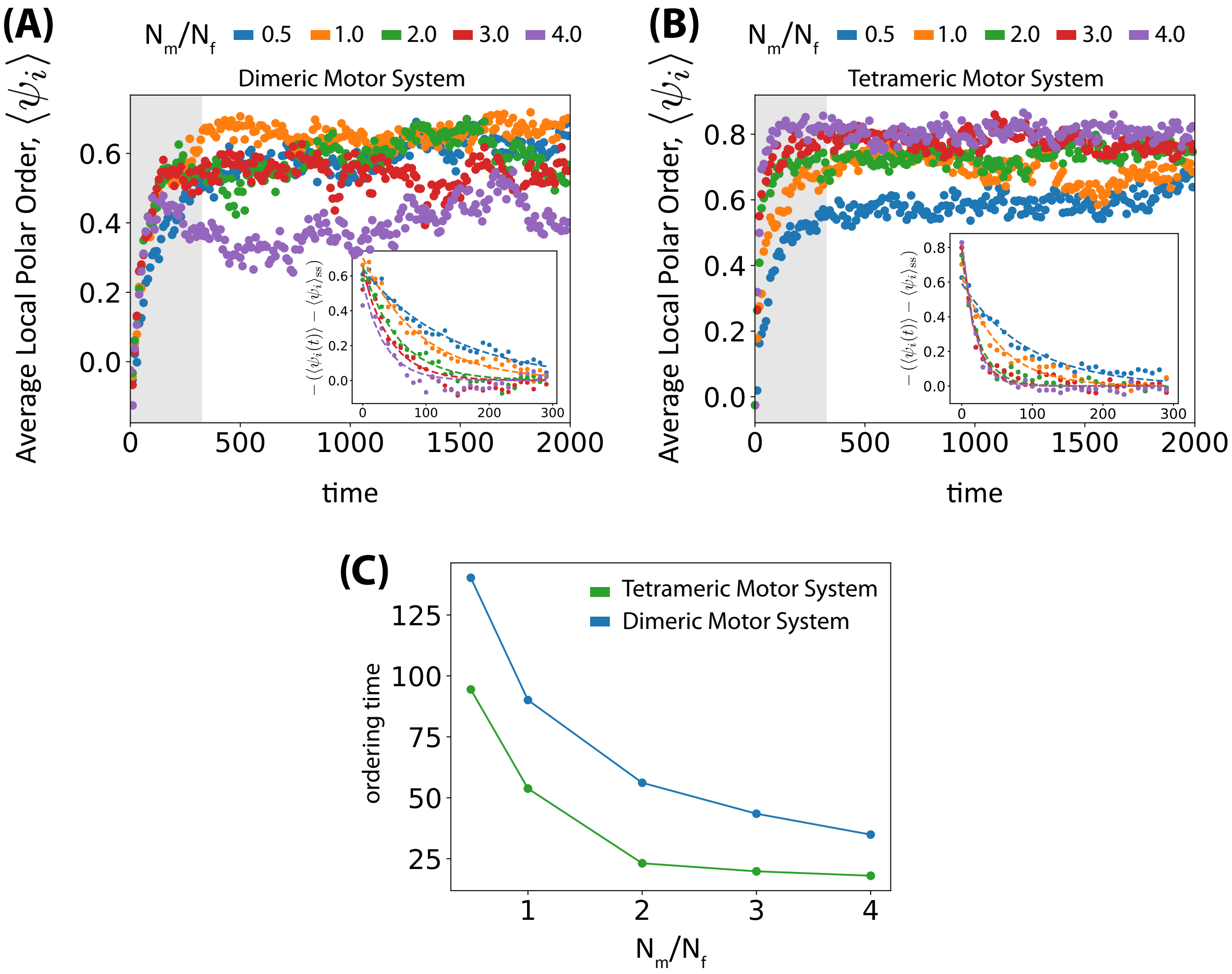

FIG. S19. Estimation of time taken to form structures for dimeric and tetrameric motor systems for different motor concentrations. The system evolves from the initial state of an equilibrated no motor system. The average local polar order $\langle\psi_i\rangle$ is the mean ψ_i of all MTs in the system at a given time. This is seen to fluctuate about a fixed value for both dimeric (A) and tetrameric (B) motor systems. Assuming that the ordering only happens initially, we fit a decaying exponential, $A\exp\left(-t/\lambda\right)$ to this data, $-\left(\langle\psi_i(t)\rangle - \langle\psi_i\rangle_{\rm ss}\right)$ (insets). $\langle\psi_i\rangle_{\rm ss}$ is the steady state, average local polar order obtained from the last 1000 steps. (C) λ is reported as the ordering time as a function of different motor concentrations. Ordering time is normalised by, τ, the timescale for the onset of activity. Area fraction is 0.74, $R_{\rm W}/r_{\rm min} = 80$, $\epsilon_{\rm w} = 8k_{\rm B}T$, $E_{\rm A} = 0.2k_{\rm B}T$, $v_{\rm m}\tau/r_{\rm min} = 50$ and $k_{\rm m}d_{\rm t}/f_{\rm s} = 1$, as per simulations presented in the main text.

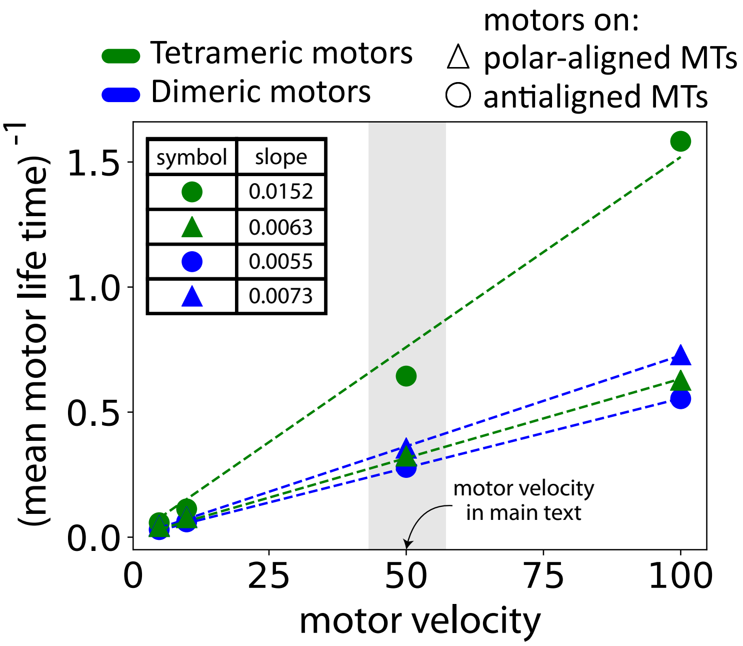

FIG. S20. Inverse of mean motor life time as a function of motor velocity for tetrameric and dimeric motors. Mean motor life time is obtained by fitting an exponential function, $A \exp\left(-t_{\mathrm{mp}}/\lambda_{\mathrm{mp}}\right)$ to the histogram of motor processivity. t_{mp} and λ_{mp} is the motor processivity and the fitting parameter to obtain mean motor life time respectively. Mean motor life time is measured in units of τ. $\lambda_{\mathrm{mp}}^{-1}$ is plotted against motor velocity, and we report the slopes of linear fits in the table. We treat motors on polar-aligned MTs and antialigned MTs separately. Motor velocity is given as $v_{\mathrm{m}}\tau/r_{\mathrm{min}}$. Area fraction is 0.74, $R_{\mathrm{W}}/r_{\mathrm{min}} = 80$, $\epsilon_{\mathrm{w}} = 8k_{\mathrm{B}}T$, $E_{\mathrm{A}} = 0.2k_{\mathrm{B}}T$, $N_m/N_f = 1$ and $k_{\mathrm{m}}d_{\mathrm{t}}/f_{\mathrm{s}} = 1$.

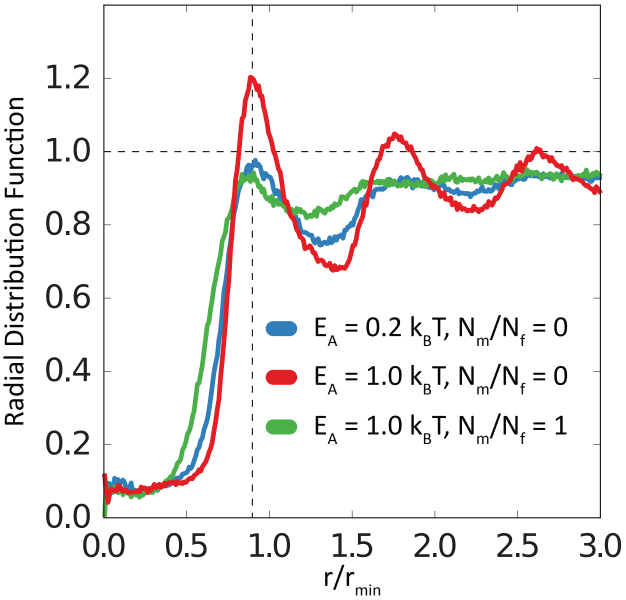

FIG. S21. Time-averaged radial distribution function of beads that make up MTs. We used dimeric motors for the curve which has $N_\mathrm{m}/N_\mathrm{f} = 1$. The beads belonging to the same MT as the bead in question were omitted for this calculation. The first peak occurs in the same point as the energy well indicated in Fig. S2. The beads which are at overlapping distances $(0.0 < r/r_\mathrm{min} < 0.5)$ occur near the confining wall due to the high attraction potential. The plot is normalised with the packing fraction of beads within the confinement.

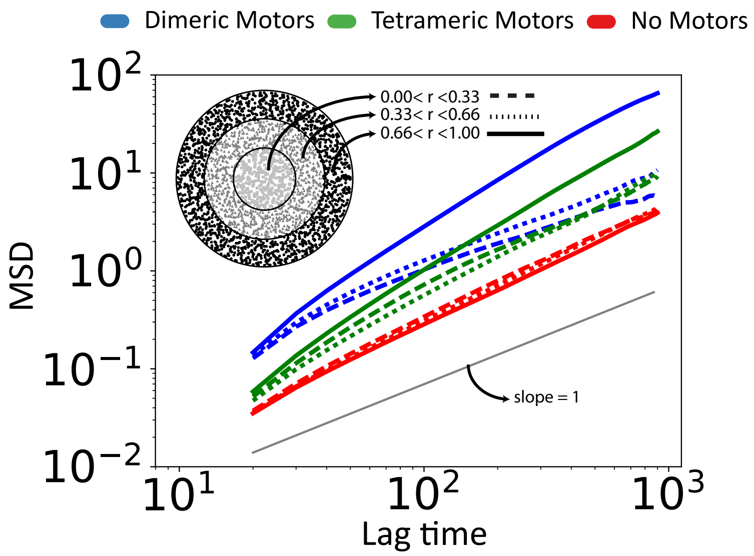

FIG. S22. Translational mean squared displacement (MSD) of MTs' center of masses by region. $E_{\mathrm{A}} = 0.2k_{\mathrm{B}}T$ and $N_{\mathrm{m}}/N_{\mathrm{f}} = 1$. The confinement is split into three sections, as illustrated in the inset. MTs whose centers of masses fall inside each of these sections at various time origins is used as a reference point to compute the MSD. If an MT leaves its original section, we continue to track it according to its position at the time origin. The region closest to the wall is the most dynamic in the cases with the tetrameric and dimeric motors. MSD is normalized using L^2. Lag time is normalised using the onset of the activity time scale, τ. The radial distance of the MT's center of mass, r is normalised by the radius of the confinement, R_{W}.

S.VI. SUPPLEMENTARY VIDEOS

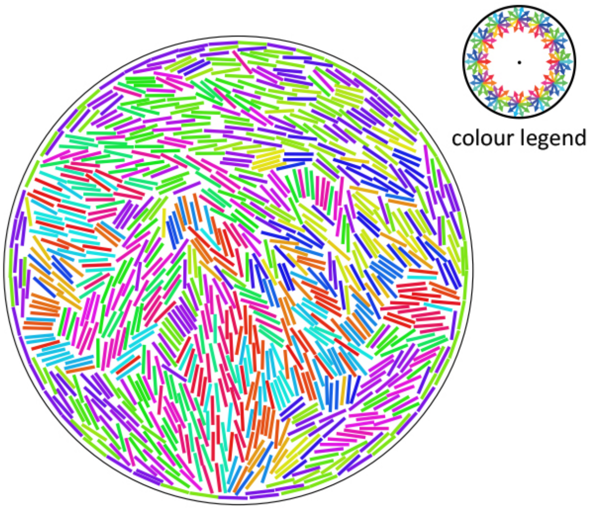

MOVIE S1. No motor system. Video shows the evolution of the system beginning from the random initial condition. The number on the top of the video is time in units of τ. Length units shown in the video are in terms of $r_{\min}$. $E_{\mathrm{A}} = 0.2 k_{\mathrm{B}} T$ and $N_{\mathrm{m}}/N_{\mathrm{f}} = 0$.

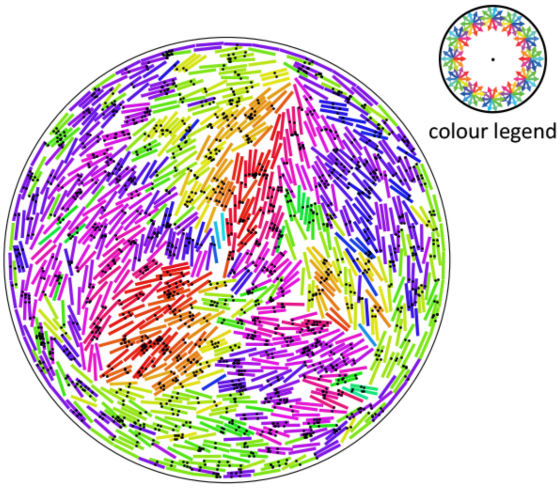

MOVIE S2. Dimeric motor system. Video shows the evolution of the dimeric motor system beginning from the random initial condition. The number on the top of the video is time in units of τ. Note the fast moving MTs at the edge of the confinement. Length units shown in the video are in terms of $r_{\min}$. $E_{\mathrm{A}} = 0.2 k_{\mathrm{B}} T$ and $N_{\mathrm{m}}/N_{\mathrm{f}} = 1$.

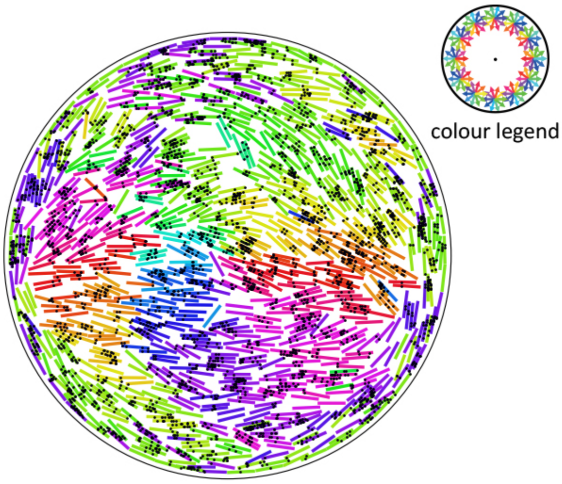

MOVIE S3. Dimeric motor system, at higher motor concentration. Video shows the evolution of the dimeric motor system beginning from the random initial condition. The number on the top of the video is time in units of τ. Note the fast moving MTs at the edge of the confinement. There are more spaces in between clusters since a higher concentration of motors binds MTs closer to each other. Length units shown in the video are in terms of r_{min}. $E_{\mathrm{A}} = 0.2k_{\mathrm{B}}T$ and $N_{\mathrm{m}}/N_{\mathrm{f}} = 2$.

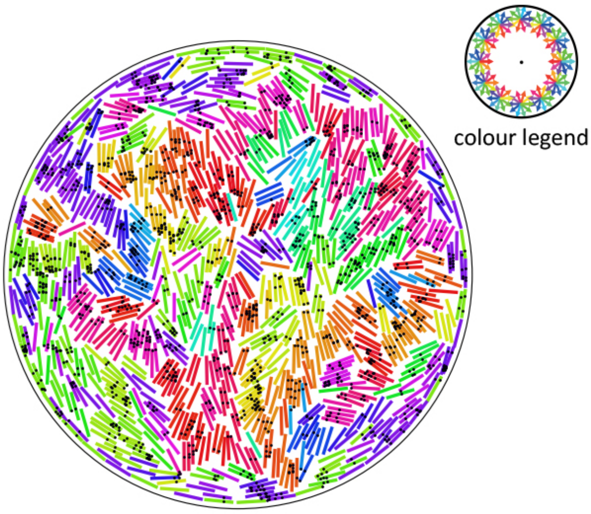

MOVIE S4. Tetrameric motor system. Video shows the evolution of the tetrameric motor system beginning from the random initial condition. The number on the top of the video is time in units of τ. Length units shown in the video are in terms of r_{min}. $E_{\mathrm{A}} = 0.2k_{\mathrm{B}}T$ and $N_{\mathrm{m}}/N_{\mathrm{f}} = 1$.

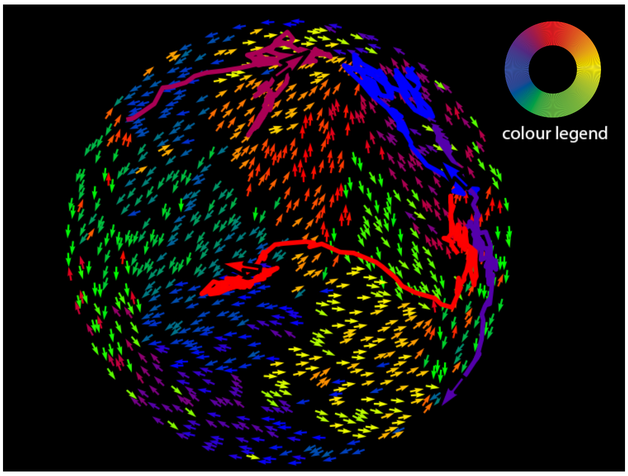

MOVIE S5. Dimeric motor system with trajectory of four probe MTs. The video corresponds to Fig. 8 in the main text. $E_\mathrm{A} = 0.2 k_\mathrm{B} T$ and $N_\mathrm{m}/N_\mathrm{f} = 1$.

SUPPORTING REFERENCES

[1] Howard, J., 2001. Mechanics of motor proteins and the cytoskeleton. Sinauer Associates Sunderland, Massachusetts.

[2] Hilitski, F., A. R. Ward, L. Cajamarca, M. F. Hagan, G. M. Grason, and Z. Dogic, 2015. Measuring Cohesion between Macromolecular Filaments One Pair at a Time: Depletion-Induced Microtubule Bundling. *Phys. Rev. Lett.* 114.

[3] Elgeti, J., and G. Gompper, 2013. Wall accumulation of self-propelled spheres. *EPL* 101:48003.

[4] Lu, W., M. Winding, M. Lakonishok, J. Wildonger, and V. I. Gelfand, 2016. Microtubule–microtubule sliding by kinesin-1 is essential for normal cytoplasmic streaming in Drosophila oocytes. *Proc. Natl. Acad. Sci. U.S.A.* 113:E4995–E5004.

[5] Löwen, H., 1994. Brownian dynamics of hard spherocylinders. *Phys. Rev. E* 50:1232–1243.

[6] Howard, J., A. J. Hudspeth, and R. D. Vale, 1989. Movement of microtubules by single kinesin molecules. *Nature* 342:154–158.

[7] Chrétien, D., and R. H. Wade, 1991. New data on the microtubule surface lattice. *Biol. Cell* 71:161–74.

[8] Wirtz, D., 2009. Particle-tracking microrheology of living cells: principles and applications. *Annu. Rev. Biophys* 38:301–26.

[9] Brady, S. T., K. K. Pfister, and G. S. Bloom, 1990. A monoclonal antibody against kinesin inhibits both anterograde and retrograde fast axonal transport in squid axoplasm. A monoclonal antibody against kinesin inhibits both anterograde and retrograde fast axonal transport in squid axoplasm. *Proc. Natl. Acad. Sci. U.S.A.* 87:1061–5.

[10] Schliwa, M., editor, 2003. Molecular Motors. Wiley-VCH, Weinheim.

[11] Crevel, I., N. Carter, M. Schliwa, and R. Cross, 1999. Coupled chemical and mechanical reaction steps in a processive Neurospora kinesin. *EMBO J* 18:5863–5872.

[12] Coppin, C. M., J. T. Finer, J. A. Spudich, and R. D. Vale, 1995. Measurement of the isometric force exerted by a single kinesin molecule. *Biophys. J.* 68:242S.

[13] Gao, T., R. Blackwell, M. A. Glaser, M. D. Betterton, and M. J. Shelley, 2015. Multiscale Polar Theory of Microtubule and Motor-Protein Assemblies. *Phys. Rev. Lett.* 114:048101.